

# Numerical Simulations of a Co-Axial Supersonic-Combusting Free-Jet Experiment

Richard L. Gaffney, Jr.

*NASA Langley Research Center, Hampton, Virginia, 23681*

## ABSTRACT

CFD calculations using the Reynolds-averaged Navier-Stokes equations coupled with species continuity equations have been made for a supersonic coaxial-jet CFD-validation experiment to determine the sensitivity of the external flowfield to the main-nozzle exit profile. Four different nozzle exit profiles were used in the study: a uniform profile, one computed using only the nozzle geometry, one computed using the nozzle geometry and part of the upstream facility combustor, and one using the nozzle and the full facility combustor. Two cases were examined using the four profiles: a non-reacting case without coflow and a reacting case with hydrogen coflow. Results show that the nozzle exit profile has a significant effect on the external flowfield. The uniform profile produced the longest jet while the profile created with the full combustor produced the shortest jet. The nozzle-only and part-combustor profiles fell between the other two profiles. The reacting flow was found to be more sensitive to the nozzle exit profile since it affects the downstream mixing and combustion. These calculations indicate the importance of properly setting the nozzle-exit profile for this type of calculation.

## INTRODUCTION

The numerical simulation of high-speed, chemically-reacting flow fields is very challenging due to the large number of physical phenomena involved in these types of flows. The development and validation of the physical models in the CFD codes used for these simulations is also challenging due, in part, to the lack of detailed and complete experimental data sets in supersonic combusting flows. To address this second challenge, the Office of the Secretary of Defense has sponsored, with contributions by NASA, a co-axial supersonic-combusting free-jet experiment in which simultaneous, instantaneous, co-located measurements of a number of flow properties have been taken.<sup>1-8</sup> CFD using the Reynolds-averaged Navier-Stokes equations coupled with species continuity equations was used to help design the experiment and identify CFD validation needs.<sup>9</sup>

During the design phase of the experiment, the importance of properly specifying the CFD boundary conditions was recognized. However, it was also recognized that not every property could be measured to the degree needed to accurately set boundary conditions. To be a proper validation experiment, the flowfield parameters of interest should not be sensitive to assumptions made to set the boundary conditions, otherwise the comparison between CFD and data depends too much on the cleverness of the person setting the boundary conditions. This may require the boundary conditions to be moved to a location where assumptions have a minimum effect on the solution. This, in turn, may increase the size of the computational domain, increase geometric complexity and/or add additional physical processes. In spite of this, if the required experimental data is lacking, then a numerical study must be undertaken to determine the sensitivity of the CFD solution to assumptions made in setting boundary conditions. Towards that end, this paper presents CFD results of both a non-reacting, mixing-only case and a chemically-reacting case, and includes an investigation of the importance of including the facility combustor and the internal nozzle flows in the calculations.

---

Approved for public release; distribution is unlimited.

This effort was performed under the sponsorship of the Defense Test Resource Management Centers (DTRMC) Test and Evaluation/Science and Technology (T&E/S&T) program, under the Hypersonic Test focus area, and by NASA's Fundamental Aeronautics Program, Hypersonics Area.

## GEOMETRY AND GRIDS

The experiment was conducted in the Direct-Connect Supersonic-Combustion Test Facility (DCSCTF)<sup>10</sup> at NASA Langley Research Center. The co-axial jet hardware, shown installed in the DCSCTF in Figure 1, is mated to the facility combustor, which provides hot vitiated air for the main jet. The flow from the main and coflow nozzles exhaust directly into the ambient air of the test cell. At the downstream end of the test cell, an open pipe connected to a 70-foot diameter vacuum sphere, draws jet gases out of the room. To prevent the inadvertent buildup of combustible gases during operation, a large fan draws outside air into the room and vents it to the roof.

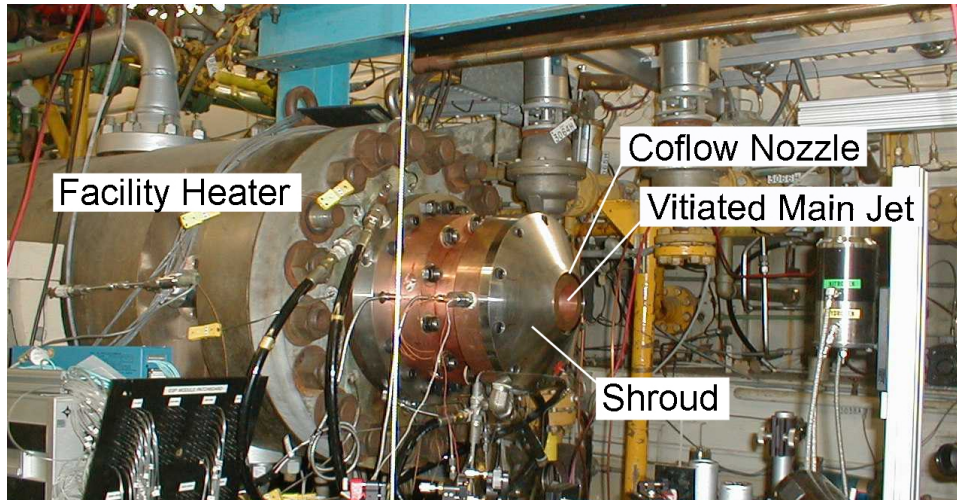


Figure 1: Experiment in the Langley Direct-Connect Supersonic-Combustion Test Facility

To simplify the numerical simulations, the computational domain was divided into internal and external parts. The internal geometry consists of the facility combustor and the main-jet nozzle. In the facility combustion-heater, oxygen is mixed with air in a plenum upstream of the combustor. From this plenum it flows through 12 holes in a baffle plate into the combustor. Hydrogen is injected into the combustor through 12 injectors that are positioned with their tips in the center of the baffle-plate holes. The injectors are smaller than the holes so that the oxygen-rich air surrounds the injected hydrogen as they enter the combustor. The axisymmetric water-cooled combustor is 51.75 inches long and has an inner diameter of 9 inches. There is a 5.75 inch long, 6.875 inch inner-diameter burner-can positioned just inside of the combustor which creates a 1.0625 inch rearward facing step downstream of the baffle plate. At the target test point, some of the steam generated in the combustion process condensed on the water-cooled combustor surface. To prevent liquid water from spraying into the test flow, a condensate trap was created by adding a 1.25 inch wide spacer with an 11.5 inch inner diameter between the combustor and the nozzle. Several small holes at the bottom of the trap allowed water to be removed during operation. The internal geometry ends with the Mach 1.6 water-cooled nozzle. This nozzle has a relatively large exit diameter (2.5 inches) to provide a large enough scale for good spacial resolution with the measurement technique. A schematic of the internal geometry is provided in Figure 2.

Because the geometry is axisymmetric, the grid is limited to a planar region extending from the axis of symmetry to either the solid walls forming the internal surfaces or the outer boundary. (Note that some figures show the solution domain and its mirror image for clarity.) The grid for the internal geometry consisted of 5 blocks. The first block filled the volume of the burner can. The second filled the volume between the burner can and the condensate trap. The third and fourth blocks filled the volume of the condensate trap, while the fifth block filled the volume of the nozzle. The block boundaries were made so that the geometry could be easily subdivided, as will be discussed further in the section on internal flow calculations. Coarse, medium and fine grids were generated for the internal geometry. The medium grid was created from the fine grid by halving the number of points in each of the two computational directions (1/4 the total number of cells). The grid spacing was adjusted on each grid level to maintain a reasonable near wall spacing ( $y^+$  in the range of 25 to 40 with peaks no greater than 90). The coarse grid was created from the medium grid in a similar fashion, with the exception of block 4, which had 85 points instead of 77 points in one of the directions. This was done to prevent a portion of the grid from being overly coarse while maintaining the target near wall spacing. Grid sizes are provided in Table 1.

The external solution domain starts at the exit of the main nozzle and extends 150 inches downstream (60 jet diameters). The outflow plane extends radially outward 100 inches (40 jet diameters). In the nozzle exit plane, there is a 0.75 inch rearward facing surface which separates the nozzle exit flow from the coflow. The exit of the coflow extends

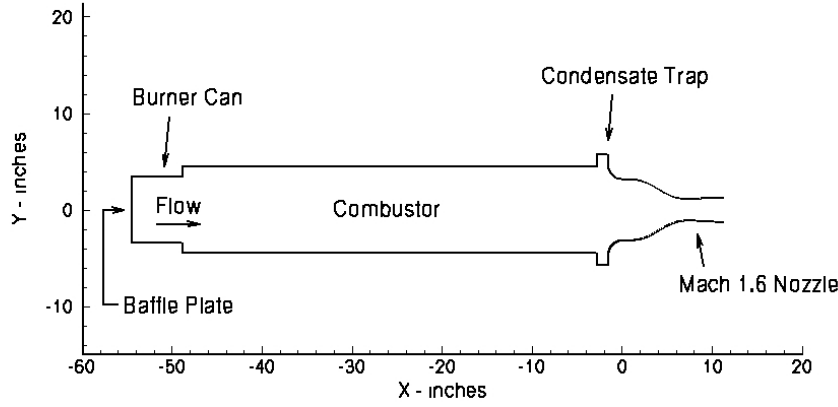


Figure 2: Internal Geometry

Block	Fine Grid	Medium Grid	Coarse Grid
1	129 x 209	65 x 105	33 x 53
2	257 x 273	129 x 137	65 x 69
3	97 x 129	49 x 65	25 x 33
4	305 x 65	153 x 33	85 x 17
5	193 x 193	97 x 97	49 x 49
Num Points	166,709	42,141	10,905

Table 1: Internal Geometry Grid Dimensions

from a radius of 2.0 to 2.25 inches. A shroud covers the hardware and extends radially outward from the outer edge of the coflow to a point with a radius of 7.5 inches and 3 inches upstream of the nozzle exit plane. The ambient-air inflow plane is 6.28 inches upstream of this point. The inflow plane extends from a radius of 7.5 inches to 125 inches. The outer boundary is sloped and connects the inflow plane at a 125 inch radius to the 100 inch radius outflow plane. The internal flowpath of the coflow is included in the external solution domain due to the subsonic injection of the coflow. The exit of the coflow is angled 15 degrees downwards towards the nozzle exit. Figure 3 shows a close-up of the nozzle-exit near-field flowpath, while Figure 4 shows the full geometry (internal and external).

The external geometry is composed of 4 blocks. The first block is the coflow plenum, while the second block is the coflow nozzle. Block 3 is a rectangular region that extends from the ambient-air inflow boundary to the corner point of the shroud and extends radially outward from the outermost portion of the shroud to the outer boundary. Block 4 is the remainder of the external flow. As with the internal flow, coarse, medium and fine grids were created for the external geometry. Also, as with the internal grids, some of the medium and coarse grid dimensions were adjusted to prevent the near wall grid spacing from becoming too large. The external grid dimensions are given in Table 2.

Grid points are clustered near the jet exit to resolve near-field flow features. The fine grid has 926 evenly spaced points in the axial direction in the first 5 jet diameters downstream of the nozzle exit. In the next 5 jet diameters there are another 330 points with a small stretching factor. The remaining 629 points in the axial direction stretch from 10 jet diameters to the outflow boundary at 60 jet diameters.

Block	Fine Grid	Medium Grid	Coarse Grid
1	49 x 129	25 x 81	25 x 41
2	65 x 65	65 x 33	33 x 17
3	65 x 385	65 x 193	33 x 97
4	1921 x 993	961 x 497	481 x 249
Num Points	1,943,124	494,332	124,556

Table 2: External Geometry Grid Dimensions

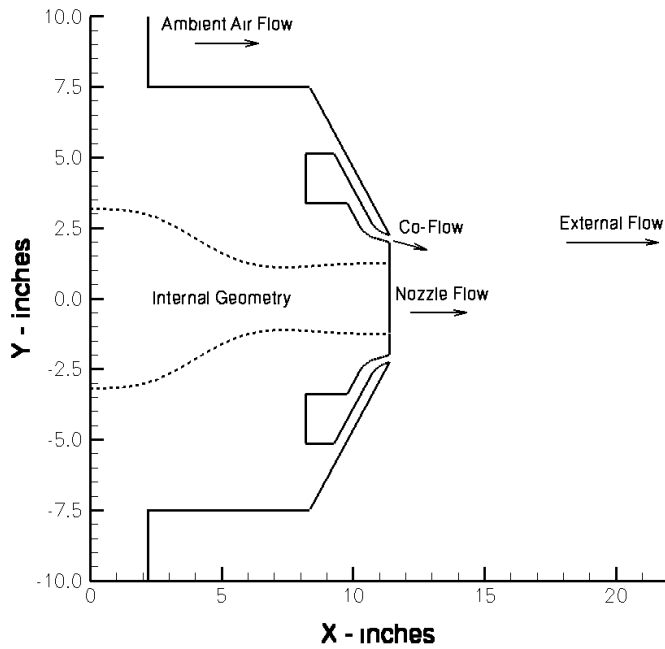


Figure 3: External Geometry Near Nozzle Exit (Dashed Internal Geometry Included For Clarity)

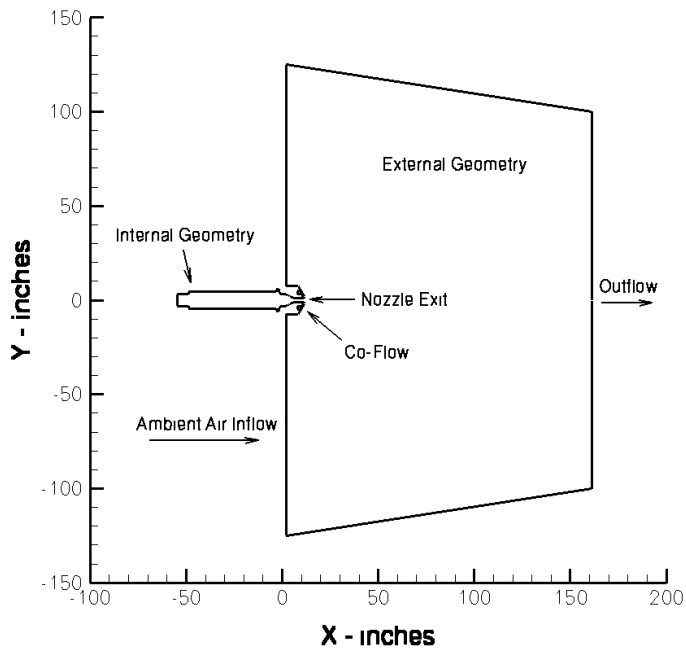


Figure 4: Full (Internal and External) Geometry

### NON-REACTING CASE

The first case investigated was a single-jet-into-ambient-air mixing-only case with no coflow injection. The facility combustion-heater was operated to provide hot vitiated air with a nozzle exit pressure of one atmosphere. Post-combustion properties in the facility combustor were computed from the mass flow rates of gases (air,  $O_2$ ,  $H_2$ ) into the

heater, assuming equilibrium chemical reaction. The gas properties and chemical composition from this calculation are given in Tables 3 and 4. To minimize computational time, minor species ( $NO$ ,  $NO_2$ ) were included in the equilibrium calculation for combustor properties but were neglected in the CFD calculations.

All the calculations presented in this paper were made using the VULCAN CFD code.<sup>11</sup> This finite-volume structured-grid code is able to solve the Reynolds-averaged Navier-Stokes equations coupled with species continuity equations and finite-rate chemical reactions. Thermodynamic properties are computed using curve fits for thermally perfect gases.<sup>12</sup> For these calculations, the Reynolds stresses were modeled using the  $k - \omega$  model of Wilcox<sup>13</sup> while gradient diffusion models with turbulent Prandtl and Schmidt numbers of 0.89 and 0.5 were used for the Reynolds heat and mass fluxes. Wall matching functions were used to reduce the near-wall grid resolutions requirements.

Property	Metric	English
Total Temperature	1,568.7 K	2,823.7 R
Total Pressure	427,473 Pa	62 psi

Table 3: Gas Properties

Species	Equil. Mass Fraction	CFD Mass Fraction
$N_2$	0.638610	0.638630
$O_2$	0.231439	0.231439
$H_2O$	0.118707	0.118707
$Ar$	0.011224	0.011224
$NO$	0.000018	-
$NO_2$	0.000002	-

Table 4: Gas Composition

## NON-REACTING INTERNAL-FLOW CALCULATIONS

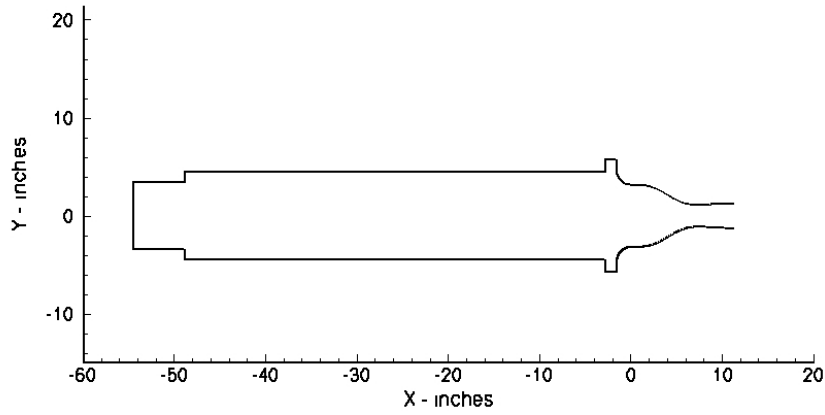
To investigate the effects of upstream geometry on nozzle exit flow and the subsequent external flowfield, three sets of calculations were made using the coarse, medium and fine grids. The first set included the full geometry, the second included the full geometry less the burner can, and the third set included only the nozzle. These three geometries are referred to as the long-combustor, short-combustor and nozzle and are shown in Figure 5. In each case the entire left-most boundary was set to a uniform, post-combustion, subsonic, inflow boundary condition. This boundary condition held the composition and total conditions constant and allowed the inflow velocity to float. Solid walls were modeled as no-slip, isothermal surfaces with a temperature of 330 K. Convergence on each of the grids and for each geometry is given in Table 5.

The solutions for the long-combustor geometry proved to be unsteady for the medium and fine grids. The source of the unsteadiness is flow structures being shed from the rearward facing step of the burner can. These can be clearly seen in Figure 6 which shows contours of the ratio of turbulent viscosity to laminar viscosity. Although the unsteady flow from the combustor would certainly introduce some unsteadiness into the external flow, solving the internal and external flows together introduces a level of complexity beyond the scope desired for this paper. Thus, for these two cases, the solution method was switched to an unsteady solution algorithm and the unsteady flow was allowed to establish over several flow-through times. The solution was then allowed to progress further in time (many more flow throughs) and the solution averaged in time. The mass flow error was monitored for the 9 cases and was less than 0.005 percent for the steady flow cases and less than 0.02 percent for the time-averaged unsteady cases.

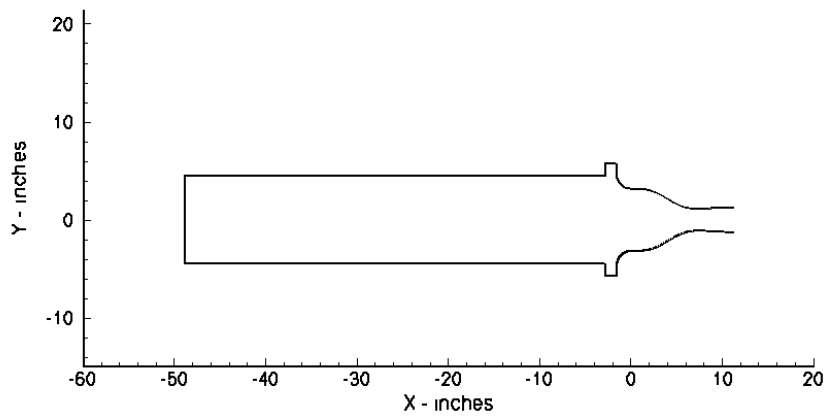
Geometry	Coarse Grid	Medium Grid	Fine Grid
Nozzle	13.888	13.754	4.068
Short Combustor	6.079	13.339	5.107
Long Combustor	5.538	(unsteady)	(unsteady)

Table 5: Residual Drop in Orders of Magnitude - Internal Geometry, Non-Reacting Cases

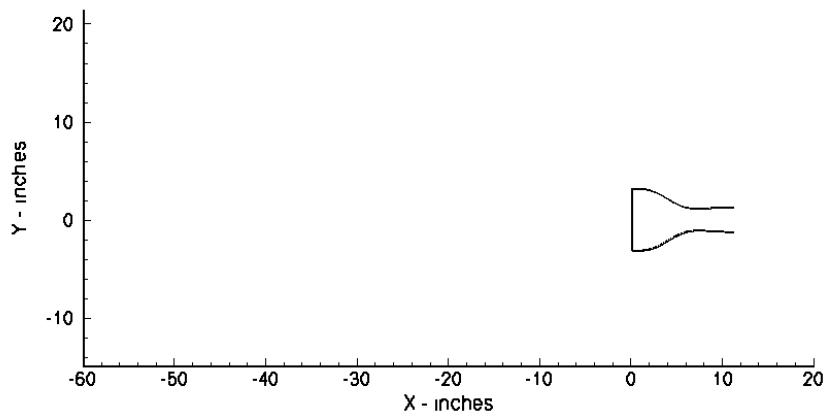
Figure 7 shows the nozzle exit profiles of the Mach number, axial velocity, static temperature and the ratio of the turbulent viscosity to the laminar viscosity. In general, the difference between the coarse, medium and fine grids is



(a) Long Combustor



(b) Short Combustor



(c) Nozzle

Figure 5: Solution Domains of the Three Internal Geometries

smaller than the difference between the geometries. The velocity and temperature profiles show significant differences in the boundary layer thicknesses between geometries. The Mach number profile has the smallest difference between the geometries due to its functional relationship with velocity and temperature. There is also a significant difference in the levels of turbulent-to-laminar viscosity ratio at the nozzle exit. The nozzle-only geometry peaks at a ratio of about 90, the short-combustor geometry peaks at about 200, and the long-combustor geometry peaks at about 1130. Figure 8 shows contours of turbulent-to-laminar viscosity ratio for all three geometries. In the nozzle case, the boundary layer

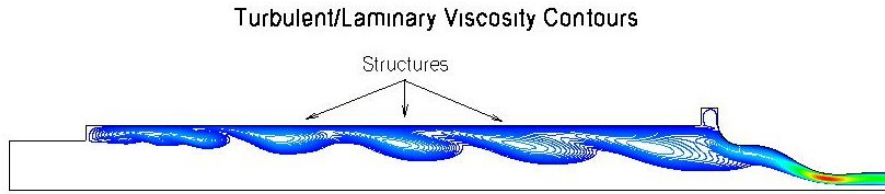


Figure 6: Snapshot of the Unsteady Flow in the Long-Combustor on the Fine Grid

begins to grow at the nozzle inflow and achieves a maximum level of viscosity ratio at the nozzle exit. For the short and long combustor geometries, the boundary layer also begins to grow at the inflow boundary but encounters downstream geometrical features (rearward facing step and condensation trap) which increase the turbulence levels. For both of these cases the viscosity ratio reaches its maximum value just upstream of the nozzle throat. The maximum levels are 324.4 and 2366.7 for the short and long combustors respectively. While the condensation trap increases the maximum viscosity ratio by a factor of about 3.6, it is the rearward facing step which has the greatest impact, increasing the viscosity ratio by a factor of 26.5 over the nozzle-only value.

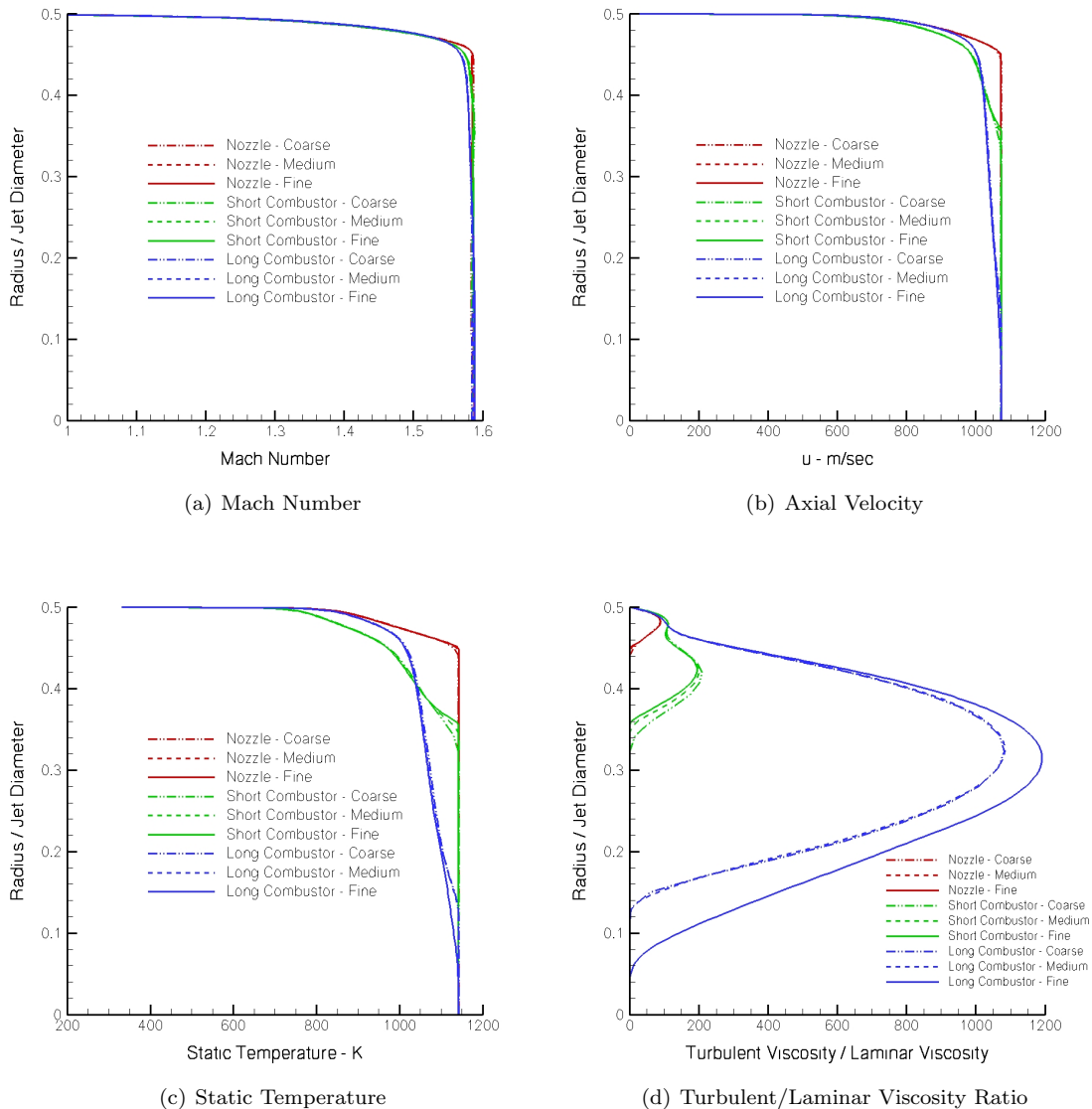
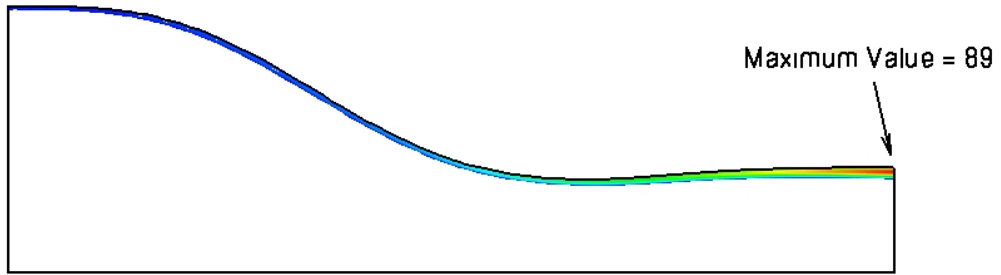
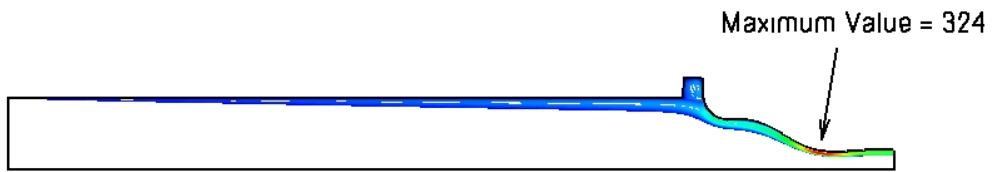


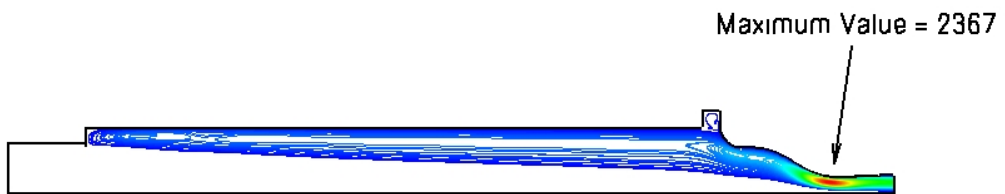
Figure 7: Profiles at the Nozzle Exit



(a) Nozzle-only



(b) Short Combustor



(c) Long Combustor (Time Averaged)

Figure 8: Fine Grid Contours of Turbulent/Laminar Viscosity Ratio

Geometry	Coarse Grid	Medium Grid	Fine Grid
Top Hat	5.344	3.568	6.880
Nozzle	5.821	6.221	5.714
Short Combustor	5.869	6.234	2.761
Long Combustor	5.826	6.016	7.155

Table 6: Residual Drop in Orders of Magnitude - External Geometry, Non-Reacting Cases

### NON-REACTING EXTERNAL-FLOW CALCULATIONS

The next step was to determine the effects of the nozzle exit profiles on the external flowfield solutions. The exit profiles from the internal flow calculations were used as a fixed inflow boundary condition for the nozzle portion of the external flow calculation. In addition to the exit properties computed from the three internal flow calculations, a top-hat (uniform) profile was added to the run matrix. The uniform properties were derived by isentropically expanding the total conditions of Table 3 to a Mach number of 1.5855, setting the turbulence intensity to 0.01 and the turbulent-to-laminar viscosity ratio to 0.01. The Mach number was selected to lie within the small range of centerline exit Mach numbers of the three internal flow calculations.

To improve the numerical convergence by convecting vorticies in the ambient air out of the solution domain, a small pressure gradient was applied across the domain by setting the ambient-air inflow total pressure to 101,325 Pa and the outflow static pressure to 101,000 Pa. This resulted in a static pressure difference of 66 Pa (0.01 psi) across the domain and an ambient air flow of about 22 m/sec. Convergence on each of the grids (coarse, medium and fine) for each nozzle-exit flow profile is given in Table 6.

Figure 9 shows the flow structure of the non-reacting flow field. At these operating conditions, the nozzle is slightly underexpanded. This creates a series of expansion and compression waves which bounce back and forth between the centerline and the shear layer. These waves turn the flow alternately towards and away from the centerline as seen in the radial velocity contours in the lower half of the figure. There is an annular shear layer created between the jet and the surrounding ambient air which spreads and eventually merges at the centerline. The jet entrains the surrounding ambient flow which separates from the surface of the shroud, creating a recirculating region on the face of the shroud. For this case there was no coflow and the air in the coflow-plenum and coflow-nozzle remained stagnant.

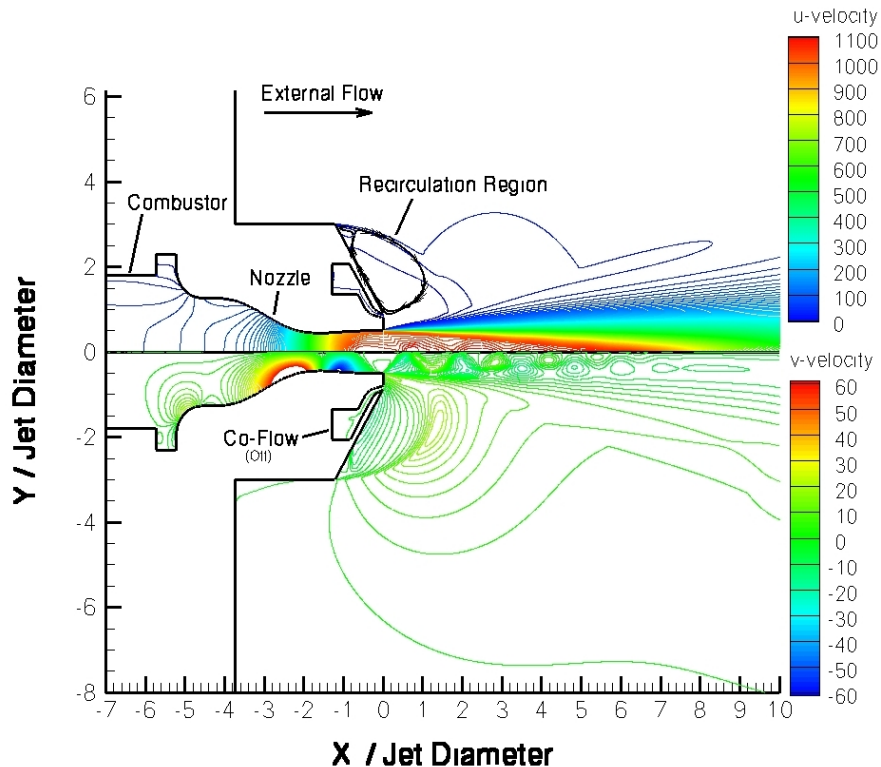


Figure 9: Non-Reacting Velocity Flow Field: Axial (u) and Radial (v) in meters/second

Figure 10 shows flow properties along the centerline. The variation of the properties in the near field are the result of the alternating expansion and compression waves previously described. In the near field, the various solutions are very similar, differing only a little in shape and amplitude. Larger differences begin to appear at axial locations greater than about 4 jet diameters. The top-hat profile shows the greatest difference from the other solutions in both wave amplitude and phase. The rapid decrease in properties between 6.7 and 11.4 jet diameters corresponds to the shear layer spreading and merging at the centerline. The axial location of the drop-off is about the same for the nozzle and short combustor geometries, is a little sooner for the long combustor and is quite a bit longer for the top-hat profile.

Figures 11-13 show radial profiles of axial velocity, static temperature and  $H_2O$  mass fraction at axial locations 1, 2, 5 and 10 jet diameters downstream of the nozzle exit. As with the centerline properties, the top-hat profile results in the least diffusive external flow while the long-combustor produces the greatest.

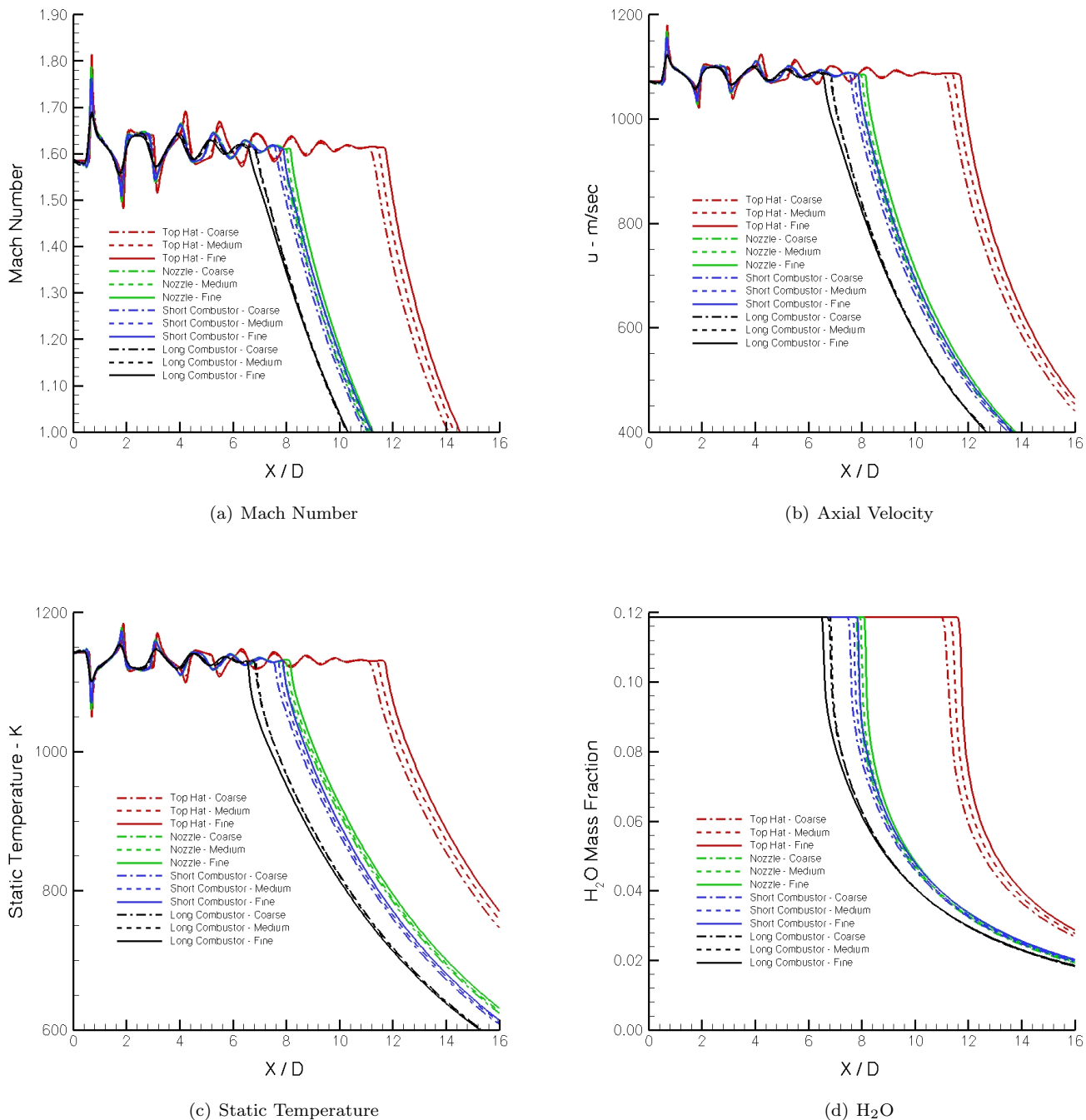
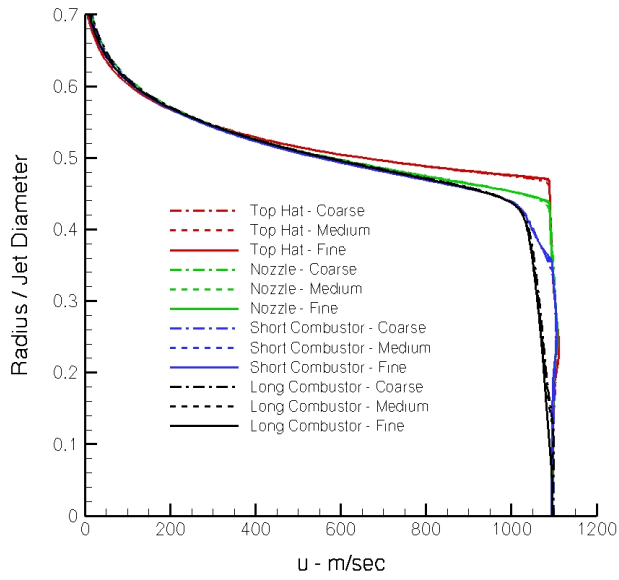
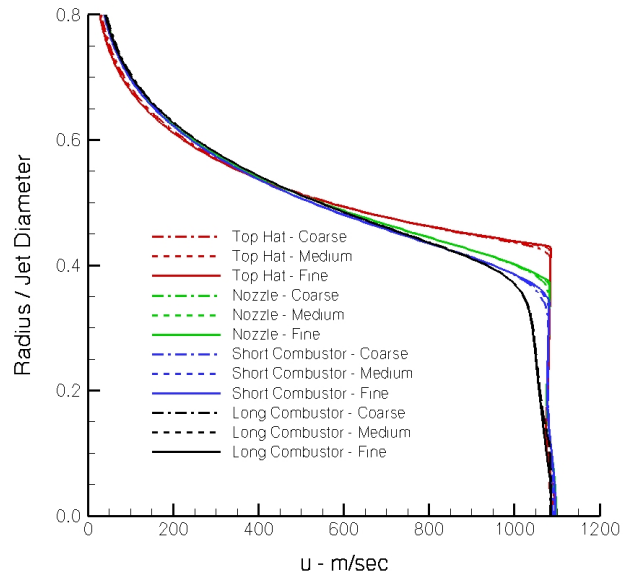


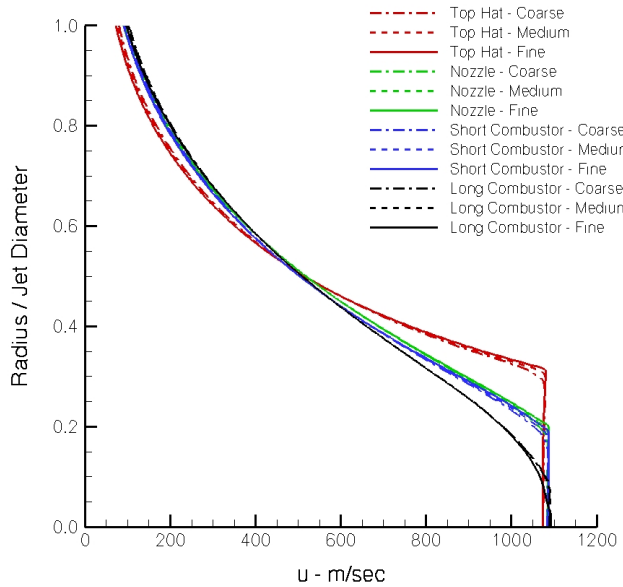
Figure 10: Non-Reacting, External-Flow Centerline Distributions



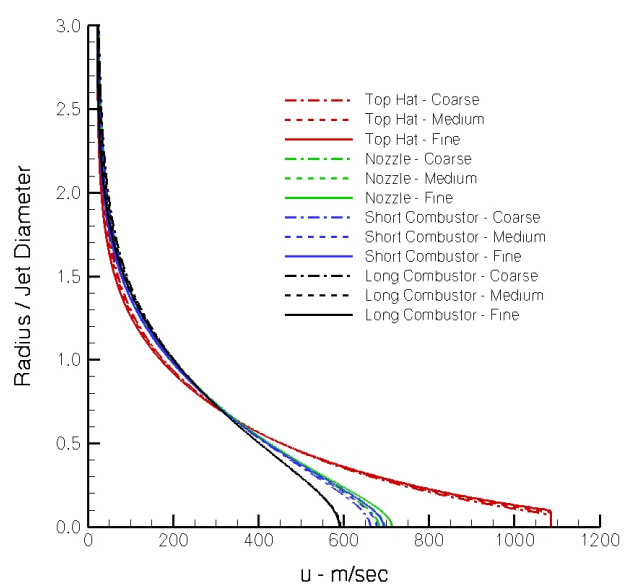
(a)  $X/D = 1$



(b)  $X/D = 2$

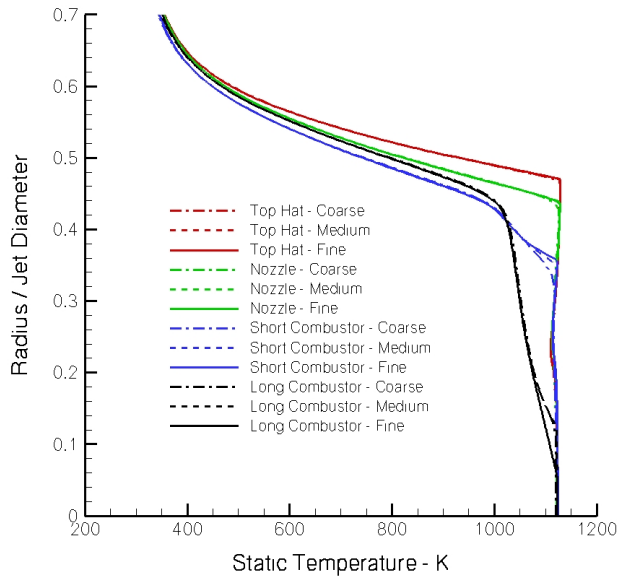


(c)  $X/D = 5$

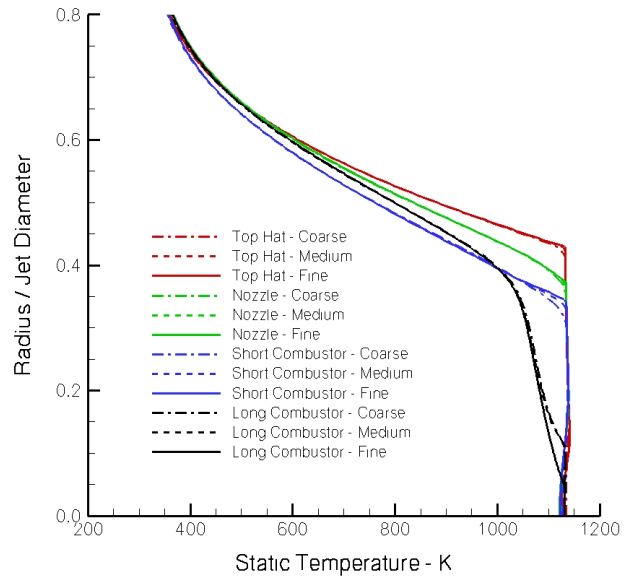


(d)  $X/D = 10$

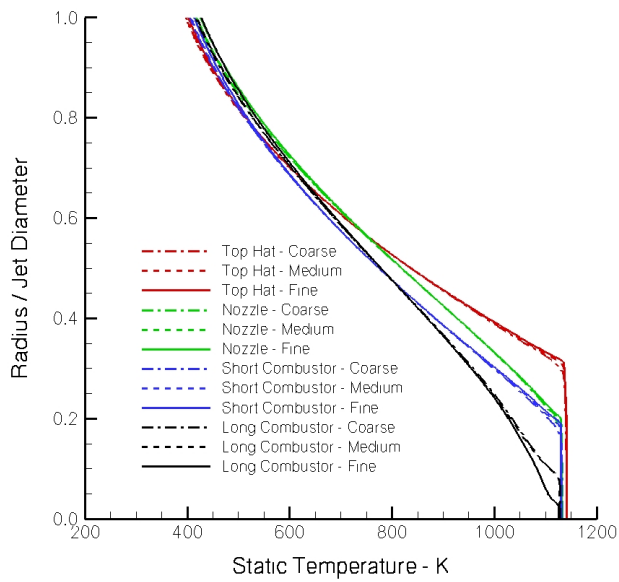
Figure 11: Non-Reacting, External-Flow Axial Velocity Profiles at Several Axial Locations



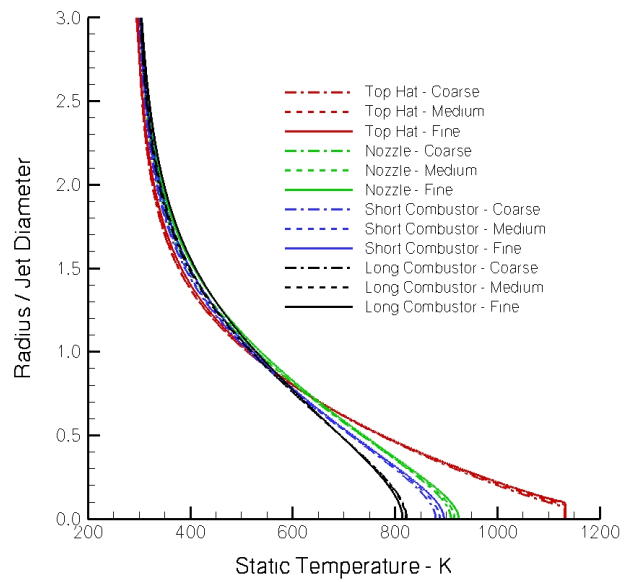
(a)  $X/D = 1$



(b)  $X/D = 2$

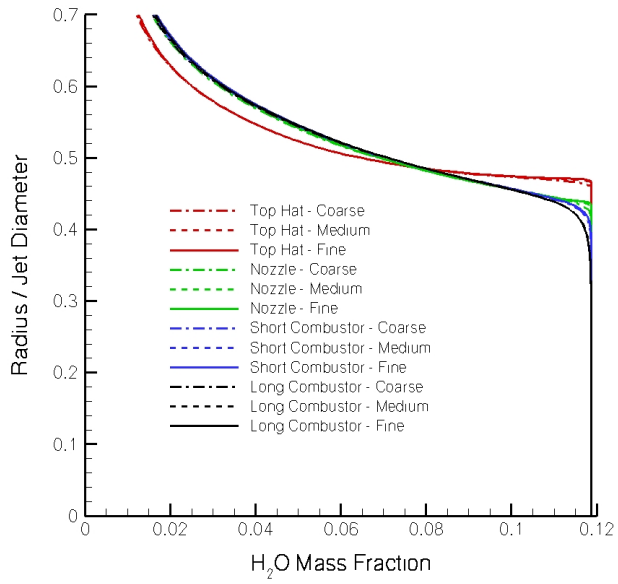


(c)  $X/D = 5$

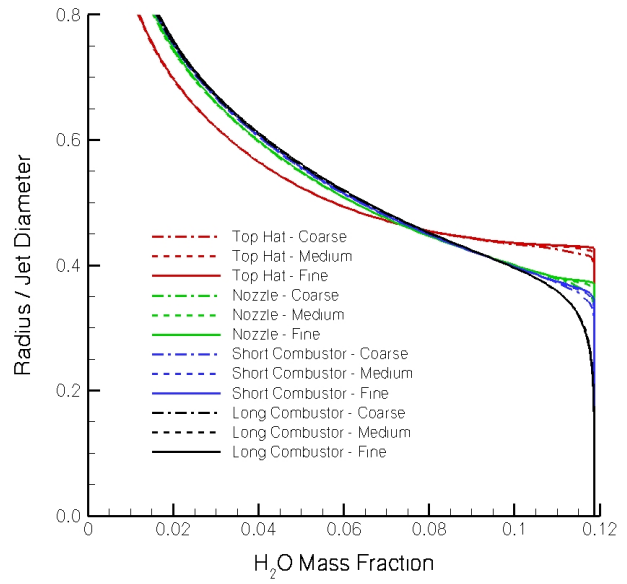


(d)  $X/D = 10$

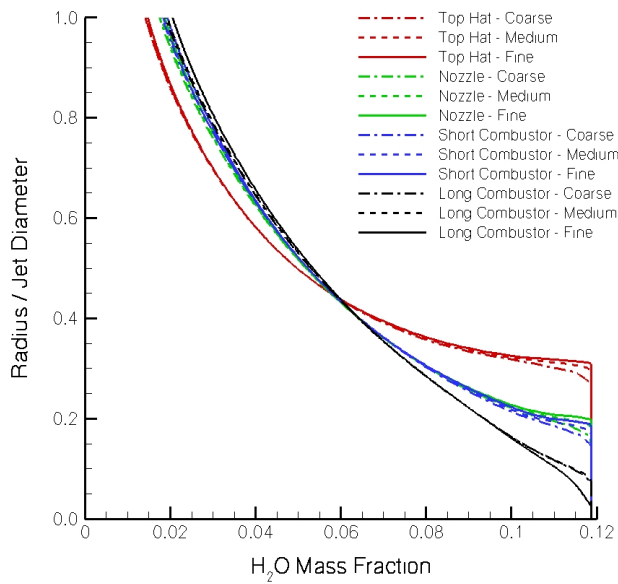
Figure 12: Non-Reacting, External-Flow Static Temperature Profiles at Several Axial Locations



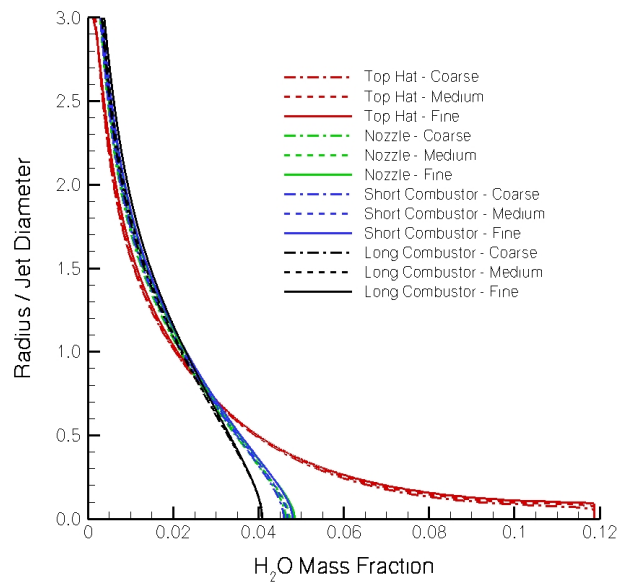
(a)  $X/D = 1$



(b)  $X/D = 2$



(c)  $X/D = 5$



(d)  $X/D = 10$

Figure 13: Non-Reacting, External-Flow  $H_2O$  Mass Fraction Profiles at Several Axial Locations

## REACTING CASE

The second case to be investigated is similar to the previous but with gaseous hydrogen flowing through the coflow nozzle at a rate of 0.0693 pounds/second. The facility combustor was operated at the same conditions used for the non-reacting, mixing-only case. These conditions give an equivalence ratio (based on the main jet and coflow) of approximately 1. For this calculation, the inflow to the coflow plenum was set to a subsonic, constant mass flow boundary condition. This boundary condition holds the composition, total temperature and mass flow constant and lets the velocity float. The total temperature of the hydrogen was set to 300 K based on the assumption that its temperature did not change from its ambient temperature storage tank. To reduce computational expenses, only the coarse grids were used for this case.

### REACTING INTERNAL-FLOW CALCULATIONS

As previously mentioned, the facility combustor operating conditions were the same as those for the non-reacting case (Table 3), however, since the external calculation would contain additional species ( $OH$ ,  $H$ ,  $O$ ), the internal flow calculations were re-computed with the additional species included. In order to avoid any inconsistency between the chemical equilibrium of the input species composition and VULCAN's hydrogen chemistry model (the 7 species / 7 reaction model), the calculations were run with finite-rate chemical reactions. This resulted in nearly constant profiles with values that differed from those of Table 4 in the 6th or 7th decimal place. The exit profiles of flow properties are identical to those of the non-reacting case (Figure 7). The convergence for the reacting, internal flow calculations are given in Table 7.

Geometry	Coarse Grid
Nozzle	13.705
Short Combustor	7.832
Long Combustor	13.591

Table 7: Residual Drop in Orders of Magnitude - Internal Geometry, Reacting Cases

### REACTING EXTERNAL-FLOW CALCULATIONS

As with the non-reacting case, a top-hat (uniform flow) nozzle-exit boundary condition was added to the external flow run matrix. All four of these cases proved to be unsteady. The source of the unsteadiness can be seen in the upper half of Figure 14 which shows a snapshot of the unsteady density contours in the near field. As with the non-reacting case, the jet entrains the ambient air flow and separates from the shroud at the corner point, creating a recirculating region on the face of the shroud. However, in this case, the flow sheds structures from the separation point. For all four of these cases, the solutions were initially run with a steady state algorithm and then switched to a time accurate algorithm. After allowing the unsteady flow field to establish, the solution was advanced further in time and the flow properties time averaged. The lower half of Figure 14 shows time averaged density contours.

The overall flow structure of the reacting case is similar to the non-reacting case, but the heat release from the chemical reactions introduces new features. Figure 15 shows time-averaged  $OH$  mass fractions and static temperature contours in the near field of the nozzle exit. The previously mentioned recirculation region pulls some of the hydrogen coflow towards the face of the shroud, creating a flame anchored to the face of the shroud near the exit of the coflow. This flame extends downstream between the coflow and the ambient air. There is a second, detached flame between the coflow and the hot vitiated air jet. These two flames merge downstream of their initial reaction points. There is also a second small recirculation region adjacent to the rearward facing surface between the main jet and coflow.

The coflow injection and subsequent combustion affects the compression and expansion wave structure within the main jet. This can be seen in the centerline properties of Figure 16. The four nozzle-exit profiles produce very-near field (first 2 jet diameters) distributions that are similar. However, downstream of this, they show significant difference in both the amplitude and frequency of the waves. As with the non-reacting case, the long-combustor shear layer diffuses to the centerline first, the top-hat last and the nozzle-only and short combustor in between the other two. A comparison of the axial location where the shear layer diffuses to the centerline between the reacting and non-reacting cases shows that the reacting-case jet extends downstream much farther than the non-reacting-case jet. For the reacting case, the shear layer/centerline merge location is between 14.3 and 18.9 jet diameters downstream of the nozzle exit, while it is only 6.7 to 11.4 jet diameters for the non-reacting case.

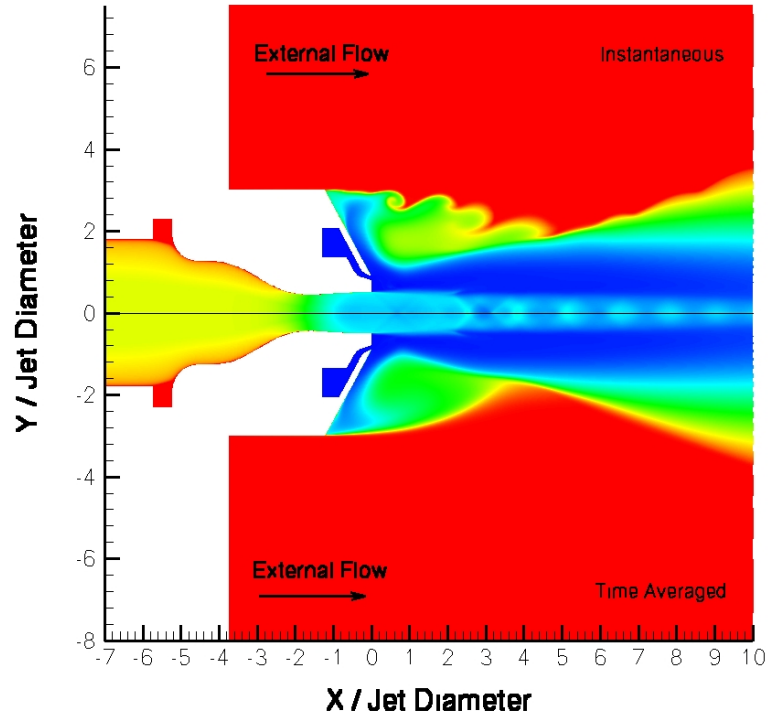


Figure 14: Instantaneous and Time Averaged Density Contours of the Nozzle-Exit Near-Field Flow, Reacting Flow Case

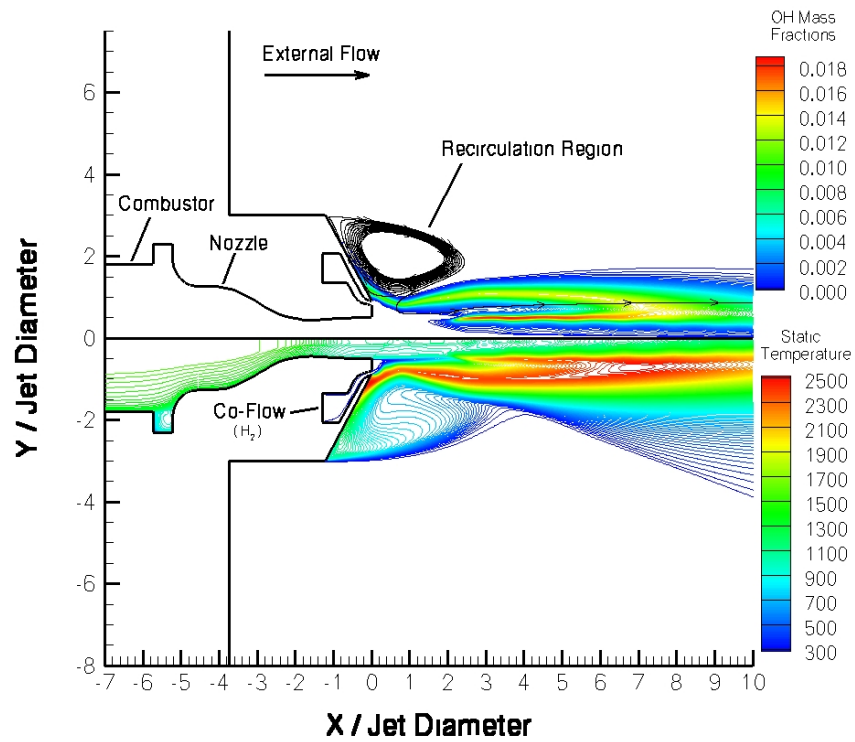
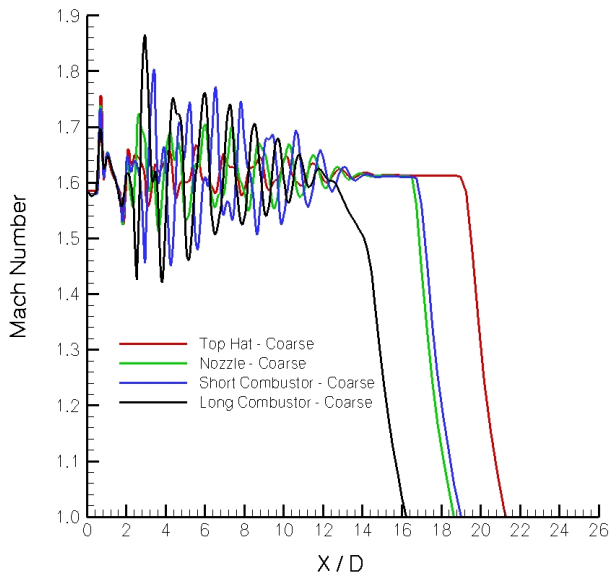
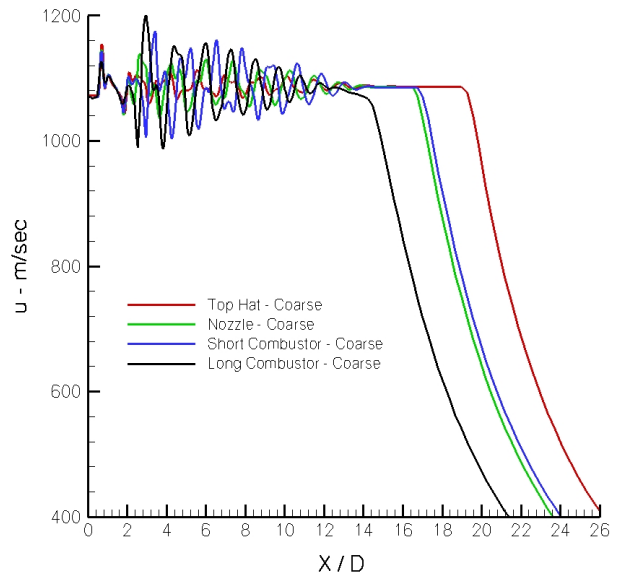


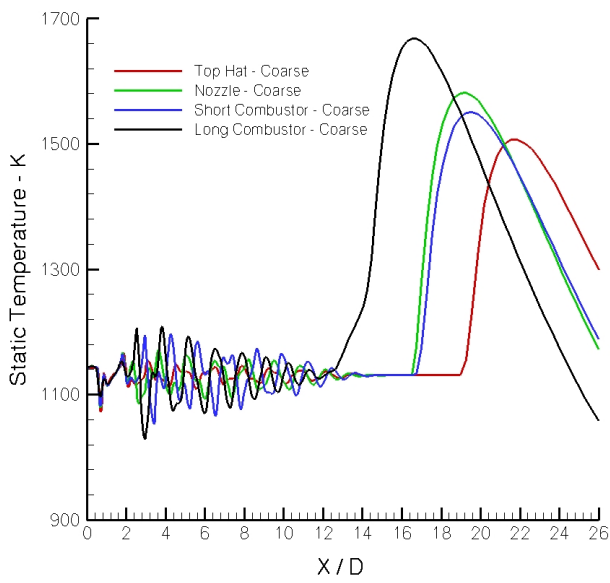
Figure 15: Reacting Flow Overview - Static Temperature in Kelvin



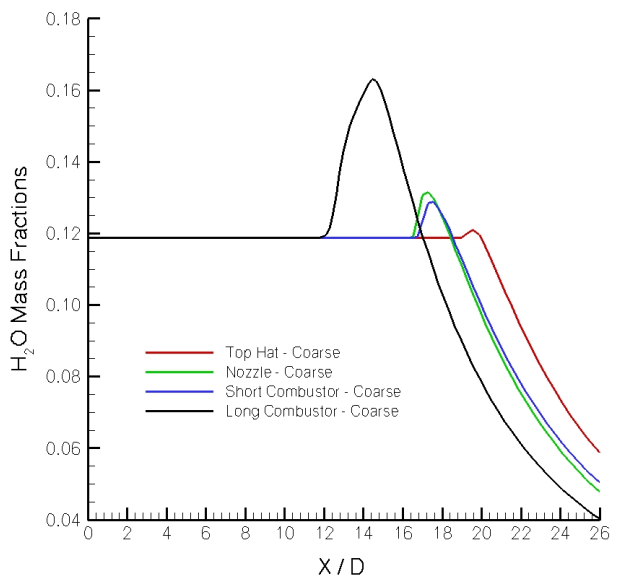
(a) Mach Number



(b) Axial Velocity



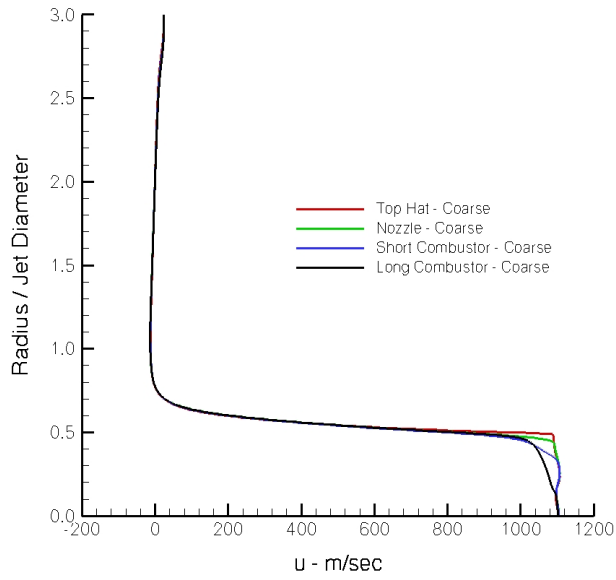
(c) Static Temperature



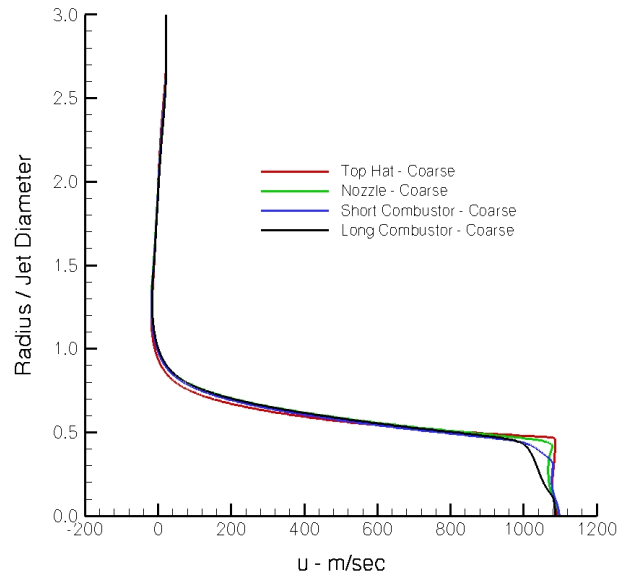
(d) H<sub>2</sub>O

Figure 16: Reacting, External-Flow Centerline Distributions

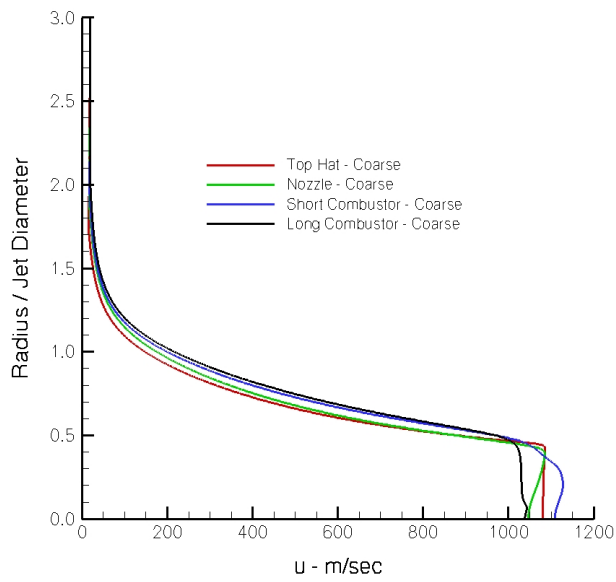
Radial distributions of axial velocity, static temperature and  $H_2O$  mass fraction are shown at several axial locations in Figures 17-19. As with the non-reacting case, the solution using the long-combustor profile has the most diffusive behavior.



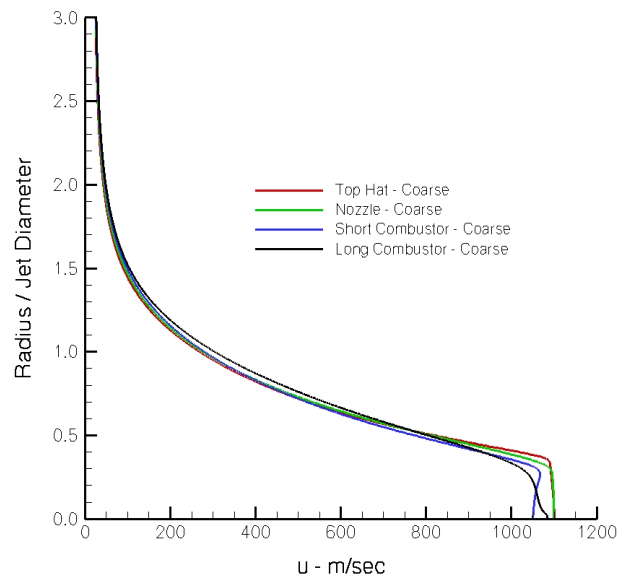
(a)  $X/D = 1$



(b)  $X/D = 2$

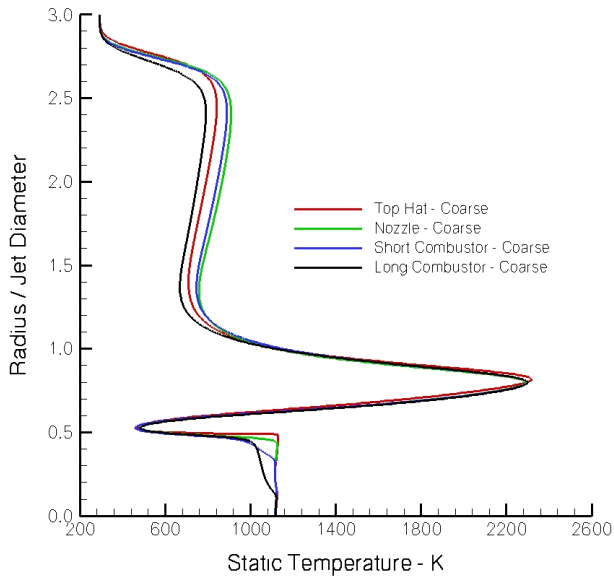


(c)  $X/D = 5$

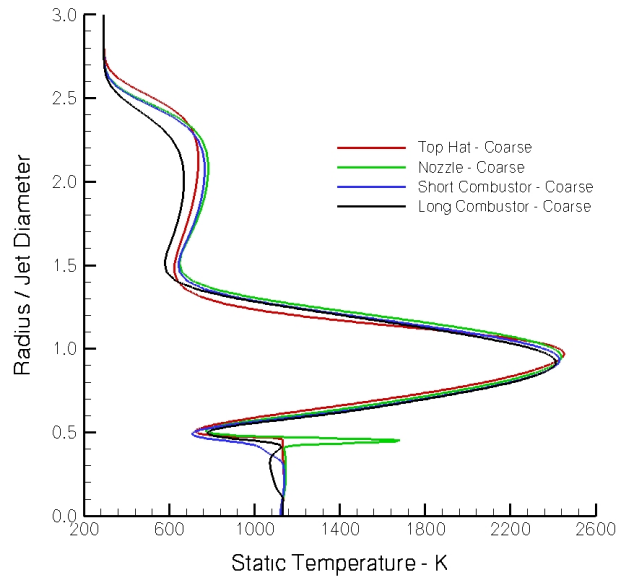


(d)  $X/D = 10$

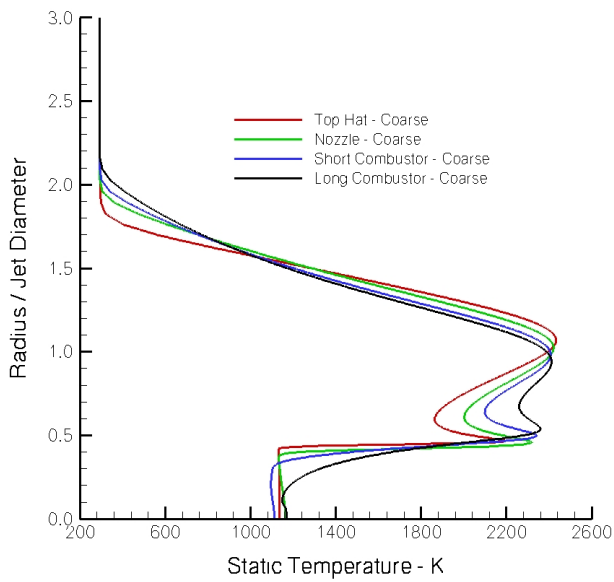
Figure 17: Reacting, External-Flow Axial Velocity Profiles at Several Axial Locations



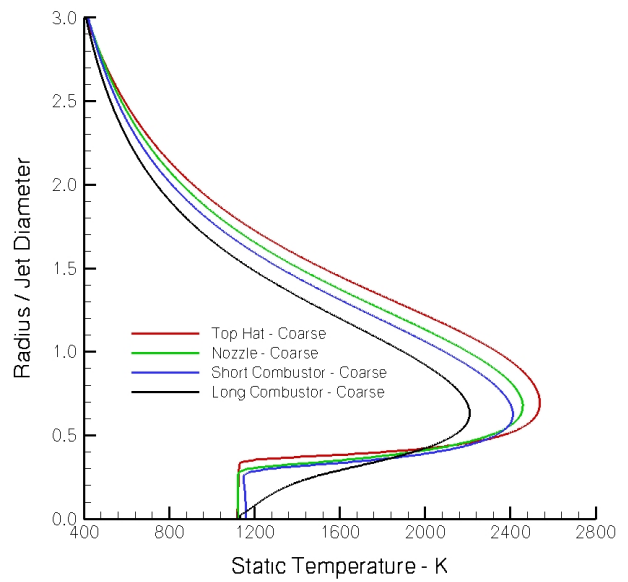
(a)  $X/D = 1$



(b)  $X/D = 2$

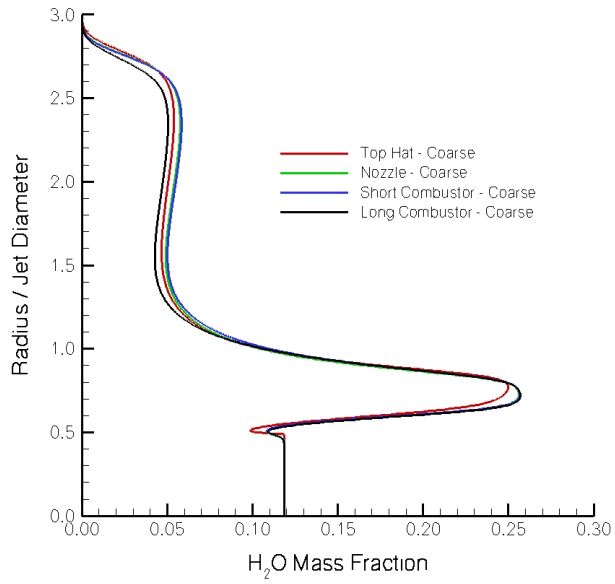


(c)  $X/D = 5$

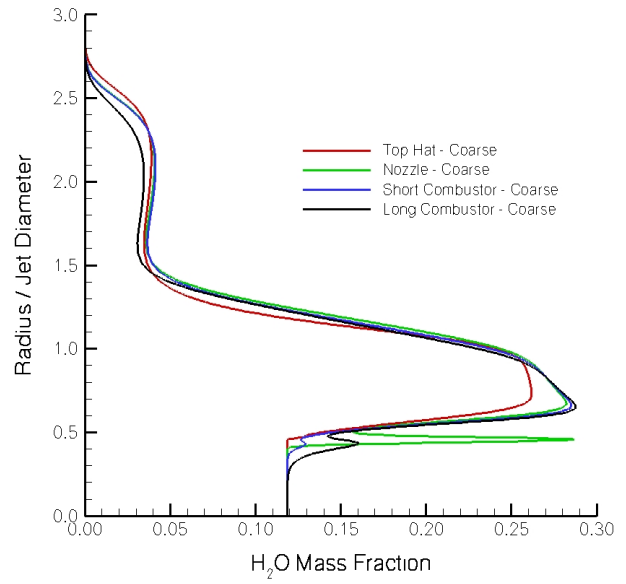


(d)  $X/D = 10$

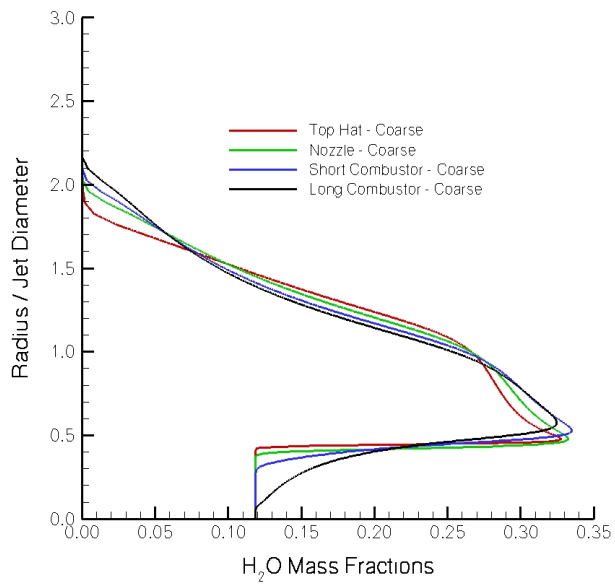
Figure 18: Reacting, External-Flow Mach Number Profiles at Several Axial Locations



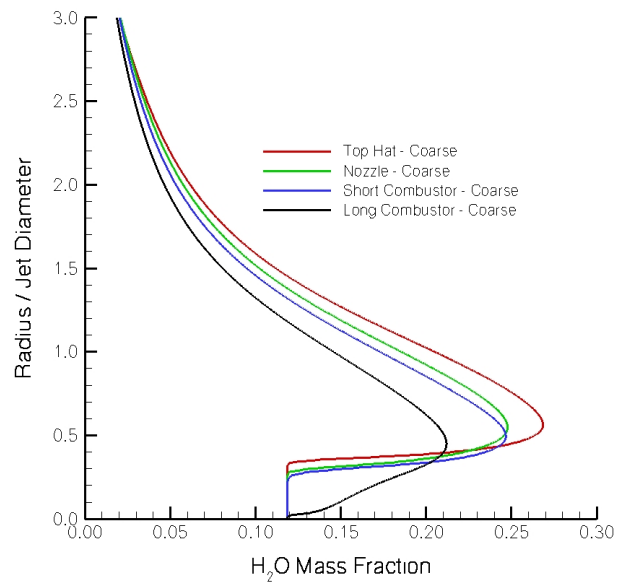
(a)  $X/D = 1$



(b)  $X/D = 2$



(c)  $X/D = 5$



(d)  $X/D = 10$

Figure 19: Reacting, External-Flow Mach Number Profiles at Several Axial Locations

## SUMMARY AND CONCLUSIONS

CFD calculations were made for a non-reacting and a reacting co-axial jet validation experiment to determine the sensitivity of the solutions to the profile in the exit plane of the vitiated-air nozzle. Four nozzle-exit profiles were used: a top-hat (uniform) profile, one computed from the nozzle geometry, one computed from the nozzle geometry and part of the upstream facility combustor, and one computed from the nozzle and the complete facility combustor. In the non-reacting case, the solutions in the near field (within the first 4 jet diameters of the nozzle exit) were similar, with the top-hat profile showing the most difference. The location where the shear layer diffused to the centerline varied significantly between the cases, varying between 6.7 and 11.4 jet diameters downstream of the nozzle exit. In the reacting case, the solutions in the very-near field (within 2 jet diameters) were similar but then varied downstream. The different profiles affected the frequency and amplitude of the compression/expansion waves inside the slightly underexpanded main jet, producing different centerline distributions. As with the non-reacting case, the location where the shear layer diffused to the centerline varied significantly between the different profile solutions, varying between 14.3 and 18.9 jet diameters downstream of the nozzle exit. These results show that the nozzle exit profile affects the downstream solution and must be taken into account when using this experiment to validate a CFD code. Although one of the nozzle exit profiles included the calculation of the facility combustor, and hence is presumably the most accurate, the calculation used a uniform, post-combustion inflow and neglected any structures or additional flow field changes due to fuel injection and combustion. A comparison with experimental data, or a more involved CFD calculation, is needed to determine if this also needs to be included in a validation calculation.

## ACKNOWLEDGMENTS

The author would like to recognize Robert Baurle of NASA Langley Research Center who, while doing a calculation of the sub-scale combustor, noticed that structures generated in the combustor persisted downstream and affected the nozzle exit profile. This raised the issue of how the nozzle exit profile affects the external jet flow. This work is a result of his observation.

## REFERENCES

- [1] Bivolaru, D., Danehy, P.M., Lee, J.W., Gaffney, R.L., Cutler, A.D., "Single-pulse, Multi-point Multi-component Interferometric Rayleigh Scattering Velocimeter," AIAA 2006-836, January, 2006.
- [2] Drummond, J.P., Danehy, P.M., Bivolaru, D., Gaffney, R.L., Parker, P., Chelliah, H.K., Cutler, A.D., Givi, P., Hassan, H.A., "Predicting the Effects of Test Media in Ground-Based Propulsion Testing," 2006 Annual ITEA Technology Review, August, 2006.
- [3] Tedder, S., Bivolaru, D., Danehy, P. M., Weikl, M.C., Beyrau, F., Seeger, T., Cutler, A. D., "Characterization of a Combined CARS and Interferometric Rayleigh Scattering System and Demonstration in a Mach 1.6 Combustion-Heated Jet," AIAA 2007-0871, January, 2007.
- [4] Drummond, J.P., Danehy, P.M., Bivolaru, D., Gaffney, R.L., Tedder, S.A., Cutler, A.D., "Modeling Combustion in Supersonic Flows," Proceedings 3rd International Symposium on Non-Equilibrium Processes, Plasma, Combustion, and Atmospheric Phenomena (NEPCAP 2007), June, 2007.
- [5] Bivolaru, D., Grinstead, K. D., Tedder S., Lee, J. W., Danehy, P.M., Cutler A. D., "Simultaneous Temperature, Concentration, and Velocity Measurements for Combustion Using CARS and Rayleigh Scattering," AIAA AMT-GT Technology Conference, June, 2007.
- [6] Drummond, J.P., Danehy, P.M., Bivolaru, D., Gaffney, R.L., Tedder, S.A., Cutler, A.D., "Supersonic combustion research at NASA," 2007 Fall Technical Meeting, Eastern States Section of the Combustion Institute, October, 2007.
- [7] Bivolaru, D., Danehy, P.M., Gaffney, R.L., Jr., Cutler, A.D., "Direct-View Multi-Point Two-Component Interferometric Rayleigh Scattering System," AIAA 2008-236, January, 2008.
- [8] Danehy, P.M., Tedder, S., Magnotti, G., Bivolaru, D., Cutler, A.D., "Simultaneous Temperature, Composition, and Velocity Measurements in a Large-scale, Supersonic, Heated Jet," 55th JANNAF Propulsion Meeting, May, 2008.
- [9] Gaffney, R. L., Jr. and Cutler, A. D., "CFD Modeling Needs And What Makes A Good Supersonic Combustion Validation Experiment," JANNAF CS/APS/PSHS/MSS Joint Meeting, June, 2005.

- [10] Guy, Robert W., Rogers, R. Clayton, Puster, Richard L., Rock, Kenneth E. and Diskin, Glenn S., "The NASA Langley Scramjet Test Complex," AIAA 1996-3243.
- [11] White, J. A. and Morrison, J. H., "A Pseudo-Temporal Multi-Grid Relaxation Scheme for Solving the Parabolized Navier-Stokes Equations," AIAA 99-3360, June, 1999.
- [12] McBride, B. J., Gordon, S. and Reno, M. A., "Thermodynamic Data for Fifty Elements," NASA TP-3287, January, 1993.
- [13] Wilcox, D. C., *Turbulence Modeling for CFD*, 2<sup>nd</sup> ed., San Diego, Ca.: DCW Industries, 2006.